

3D3C velocimetry measurements of an electrothermal microvortex using wavefront deformation PTV and a single camera

Aloke Kumar · Christian Cierpka ·
Stuart J. Williams · Christian J. Kähler ·
Steven T. Wereley

Received: 13 April 2010 / Accepted: 9 July 2010 / Published online: 28 July 2010
© Springer-Verlag 2010

Abstract We study the three-dimensional fluid transport in an electrothermal microvortex (EMV), by using wavefront deformation particle-tracking velocimetry (PTV) developed at Universität der Bundeswehr München. By using a cylindrical lens in conjunction with a microscope objective lens, systematic wavefront deformations in the particle images are created. The particles are observed by a single camera and appear as ellipses. The elliptical nature of the particle images encodes out-of-plane information regarding the particle's position. This new technique is ideally suited for measuring transport in the EMV and provides full three-dimensional, time-resolved particle trajectories with Lagrangian velocity and acceleration. Measurements reveal the toroidal nature of the EMV and the experimentally obtained velocities are used to validate a simplistic model, which describes the interaction between

the applied laser illumination and the microfluidic device. The model allows one to conduct numerical simulations of the complex fluid transport in the EMV.

1 Introduction

Recently Kumar et al. (2009) demonstrated the generation of an elegant toroidal EMV in a simple AC electrokinetic system by using laser induced electrothermal flows. Their experimental setup consisted of parallel-plate electrodes fabricated from indium tin oxide (ITO), which were biased with an AC signal, and on which highly localized infrared (IR; 1064 nm) laser illumination was shone. Compared to the visible wavelength spectrum, ITO absorbs strongly in the infrared and thus the applied optical landscape can heat the substrate generating thermal gradients. Kumar et al. (2010b) used laser-induced fluorescence thermometry to characterize these thermal gradients. They found that such focused illumination can result in an absolute temperature increase of only a few Kelvin, varying radically over tens of micrometers thus giving rise to very high temperature gradients ($\sim 10^5 \text{ K m}^{-1}$). Such optically induced gradients of temperature, either in the fluid or at fluid boundaries, in the presence of an electric field can result in electrothermal flows. Generation of three-dimensional flow structures with optically induced electrothermal flows was first observed by Mizuno et al. (1995), who used an IR laser, and later also by Green et al. (2000), who used a broad wavelength illumination source. However, unlike the latter two, the experimental setup employed by Kumar et al. (2009) does not introduce dielectrophoretic forces acting on the tracer particles. This makes possible the study of the EMV with a simple single color velocimetry technique.

Electronic supplementary material The online version of this article (doi:10.1007/s10404-010-0674-4) contains supplementary material, which is available to authorized users.

A. Kumar · S. T. Wereley (✉)
Birck Nanotechnology Center, School of Mechanical
Engineering, Purdue University, West Lafayette, IN 47907, USA
e-mail: wereley@purdue.edu

A. Kumar
Biosciences Division,
Oak Ridge National Laboratory, Oak Ridge, TN 37831, USA

C. Cierpka · C. J. Kähler
Institut für Strömungsmechanik und Aerodynamik, Universität
der Bundeswehr München, 85577 Neubiberg, Germany

S. J. Williams
School of Mechanical Engineering, University of Louisville,
Louisville, KY 40292, USA

In addition to displaying a highly three-dimensional structure, the EMV studied by Kumar et al. (2009) has important consequences for ‘lab-on-a-chip’ type of applications. Williams et al. (2008a) have demonstrated a very useful application of the EMV: they used the vortex to accumulate, translate, and pattern micro and nano-particles and concentrate them on the surface of an electrode. The EMV aids in the rapid transport of particles from the bulk fluid to the location of interest on the electrode surface, and hence the technique proposed by Williams et al. (2008a) was named rapid electrokinetic patterning (REP) (see video in Williams et al. 2008b). In another work, Kumar et al. (2010b) utilized the optical modulation of the vortex to investigate the nature of some fundamental AC electrokinetic forces at work in REP. The three-dimensional structure of the fluid flow in the EMV has extremely important consequences for REP. While fluid drag parallel to the electrode surface aids particle aggregation in REP, the perpendicular component of fluid drag can result in the appearance of critical phenomenon in REP (Kumar et al. 2010b). The existence of such a critical frequency has been used to yield a novel sorting technique (Williams et al. 2010). The EMV has also been utilized to create novel reconfigurable assemblies in a digital microfluidic system (Kumar et al. 2010a). Thus, we see that the optically modulated EMV can be applied towards a host of different applications. In order to gain a complete understanding of these applications, it is necessary to (a) visualize the EMV in 3D and (b) be able to numerically simulate the fluid transport in the EMV.

Former fluid flow visualization studies of the EMV have been restricted to two-dimensional investigations of fluid flow near an electrode surface (Kumar et al. 2009). In (Kumar et al. 2009), the researchers showed that flow in the EMV resembles a ‘sink-type’ flow in a plane parallel and close to the electrode surface. The ‘sink-type’ flow structure explained the rapid collection of particles at illuminated sites in REP. While Kumar et al. (2009) found agreement with the theory of electrothermal flows, the study only qualitatively demonstrated the three-dimensional toroidal nature of the EMV, with a large out-of-plane (z) velocity gradient and shallow depth ($\sim 25 \mu\text{m}$). The full velocity field of the EMV is yet to be resolved. The microvortex possesses an intricate three-dimensional structure necessitating a full three-dimension three-component (3D3C) velocity measurement of the vortex. However, three-dimensional velocity measurement at the micron scale is often challenging, due to the limited optical access. Nevertheless, today strong demand for reliable and easily applicable 3D flow measurement techniques exists (Lee and Kim 2009; Lindken et al. 2009). The direct adaptation of techniques used in macroscopic flow measurements for microscopic flow is often

not possible. Tomographic micron resolution particle image velocimetry (tomo- μPIV) and stereo- μPIV have proven to be promising (Lindken et al. 2006); nevertheless these techniques suffer from the difficulty of the calibration for multi camera techniques in microscopy (Cierpka et al. 2010a) and show limited accuracy (Lindken et al. 2006). To overcome these limitations, single camera velocimetry techniques were developed. One such promising approach to 3-D microfluidic measurements is the microdigital holographic particle-tracking velocimetry (PTV) (Satake et al. 2005; Yang and Chuang 2005; Sheng et al. 2006; Choi and Lee 2010). In another approach, Stolz and Kähler (1994) used defocused particle images to measure the third velocity component by PTV in a 1.5 mm thick light sheet. Recently, Peterson et al. (2008) measured velocity profiles in a channel by determining the out-of-plane position by measuring the size of the diffraction ring of the particle images. A different approach was used by Hain and Kähler (2006), who used a tilt angle between the measurement volume and the camera to create systematic image aberrations, which could be calibrated with the particles’ out-of-plane location. Optical aberrations due to uniaxial bending of a dichroic mirror were used by Ragan et al. (2006), to study the motion of kidney cells. Depth encoding using three pin-holes in front of the camera was proposed by Willert and Gharib (1992) and later Yoon and Kim (2006) successfully adopted the technique for a micro-volume. A very effective way of extending infinity corrected microscopes into the third dimension lies in the placement of a cylindrical lens in the optical path. Recently, two groups have demonstrated the applicability of such systems for resolving micron scale flows (Chen et al. 2009; Cierpka et al. 2009).

From a numerical simulation perspective, a successful numerical simulation of transport in the EMV is yet to be carried out. Successful numerical simulations are impeded by the complex energy transport and the presence of several unknown parameters. For example, the fraction of laser illumination absorbed by the substrate and the liquid are difficult to resolve and are unknown.

In this work, we employ the 3D3C μPTV using a cylindrical lens (Cierpka et al. 2010b) to investigate the EMV. Cierpka et al.’s (2010b) technique could easily be adapted to our present infrastructure, consisting of a Nikon TE2000U microscope, and a complete 3D toroidal structure of the EMV was resolved. In the absence of an accurate knowledge of energy balance, a simplistic model is introduced—that of accounting for optically induced heating by using temperature boundary conditions. The experimentally obtained velocity profiles are used to validate the model. Thus, this work fills an important gap in the understanding the EMV and its related phenomena.

2 Materials and methods

2.1 Chip fabrication and microvortex generation

The microfluidic chip consists of a microfluidic channel embedded between two parallel-plate electrodes (Fig. 1). An ITO-coated glass cover slip (SPI Supplies Inc., PA, USA), $\sim 170 \mu\text{m}$ thick, was used for the bottom electrode while the top electrode was made from ITO-coated glass ($\sim 0.7 \text{ mm}$ thick). The microfluidic chamber had a height of $\sim 50 \mu\text{m}$, and it was constructed from a spacer material with millimeter length channels. The experimental volume was placed far from channel side-walls to avoid any wall-based distortion of the local electric field. Interested readers can refer to (Kumar et al. 2009) for further details on chip fabrication. The electrodes were biased with an AC signal, resulting in a uniform electric field in the experimental area. For the present investigation, an AC voltage (V) of $8.9 V_{pp}$ (volts peak-to-peak) was applied and measurements were performed at three AC frequencies ($F = 100, 200, 300 \text{ kHz}$).

Red fluorescent carboxylate-modified polystyrene particles (Invitrogen, MD, USA) of diameter $3 \mu\text{m}$, were utilized for visualizing the EMV. A tracer laden solution was prepared by diluting $15 \mu\text{l}$ of the 2% by volume solids particle solution with 1 ml of DI water. Prior to experimentation, the tracer laden solution was introduced into the microfluidic channel. The microfluidic apparatus was mounted on an inverted Nikon TE2000U microscope and finally to initiate the EMV, a $20\times$ Nikon objective lens (0.45 NA and 2-mm WD) was used to focus an IR laser beam of wavelength 1064 nm on the top ITO glass surface (Fig. 1). Laser power values (P) stated in the text refers to the total laser power impinging on the back focal plane of the microscope objective lens. For viewing tracer particles, an epi-fluorescent filter cube (Nikon TRITC HYQ) was

employed and the fluorescent excitation was provided from a 120-W lamp (X-cite 120, Exfo, Quebec, Canada).

2.2 Wavefront deformation PTV

The velocity measurement technique applied here is based on the tracking of individual particles. A cylindrical lens (Edmond Optics, USA) with a focal length of $f_c = 150 \text{ mm}$ was placed directly in front of the camera (PCO.1600, Cooke Corporation, MI, USA). The basic principle of the optical setup is sketched in Fig. 2. Due to the cylindrical lens in the optical system the location of the focal plane in the (x, z) plane differs from the focal plane location in the perpendicular (y, z) plane. In the (x, z) plane particle A is closer to the focal plane and will be imaged with a smaller width a_x , while particle B is farther away and a_x of B will therefore be larger. In the lower part of Fig. 2, the view of the system is rotated by 90° . The curvature of the cylindrical lens causes a shortening of the distance from the lenses to the focal plane (F_{yz}), compared to the (x, z) plane. Now particle B is closer to F_{yz} , which results in a smaller image a_y , than that of particle A . The reconstructed image in both directions of the different particles A and B shows clearly the effect of the different positions according to the in-focus planes. Particles that are close to one focal plane are further away from the other and will appear with different extension in width a_x and height a_y . Thus, in the image plane, i.e. the (x, y) or (r, θ) plane, the particles appear as ellipses. Using calibration, the z -position can be determined by the elliptical nature of the particle images. By reconstruction the particles' position at two time instants t_1 and t_2 , the 3D displacement, and with known magnification the 3D velocity can be determined $\mathbf{u} = (u_r, u_\theta, u_z) = \Delta\mathbf{x}/(t_1 - t_2)$. Particle trajectories may be calculated during the whole measurement time, providing

Fig. 1 An illustration of the microfluidic chip setup. A $20\times$ Nikon microscope objective lens focuses the IR laser beam onto the top surface of the microfluidic chamber. As the same lens serves for viewing the tracer particles, the focal plane coincides with the top surface. A cylindrical lens (not shown) placed in the optical path of the imaging optics causes the particles to appear as ellipses

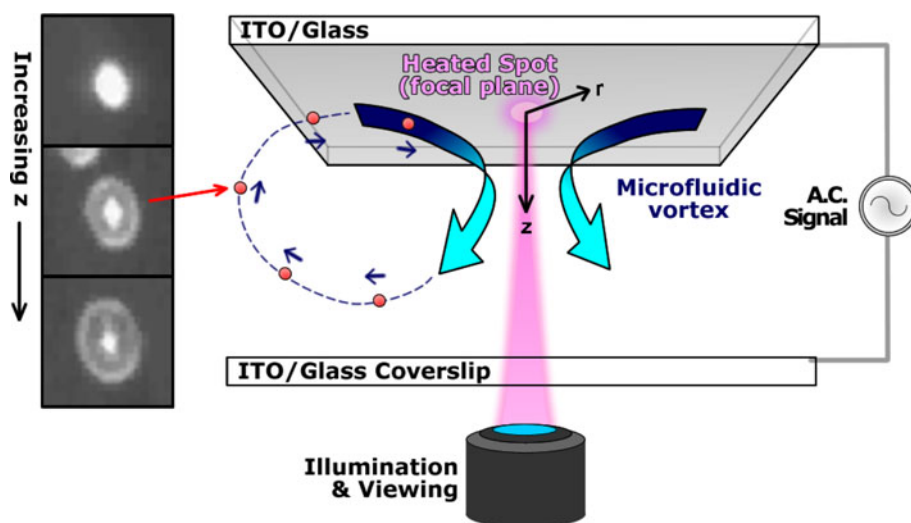
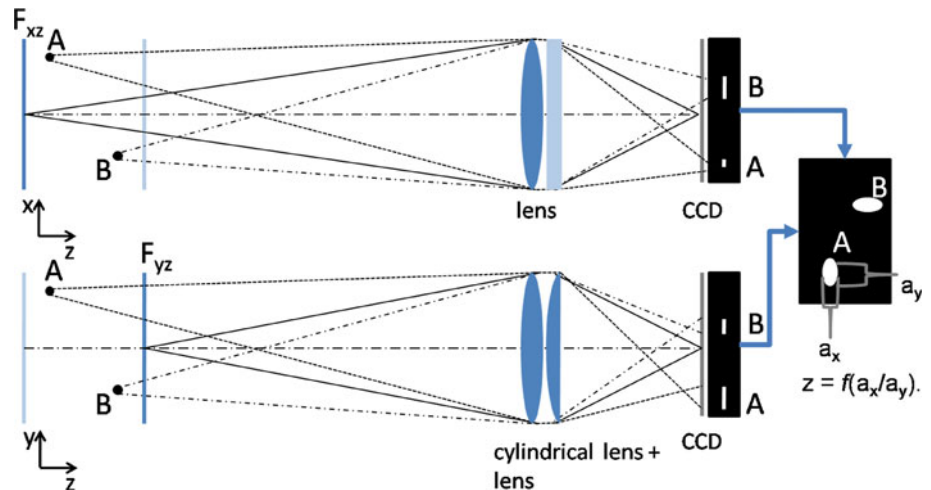


Fig. 2 Ray tracing schematic of the optical set up for the wavefront deformation PTV. In the yz -plane the additional cylindrical lens shortens the distance to the in-focus plane F_{xz}



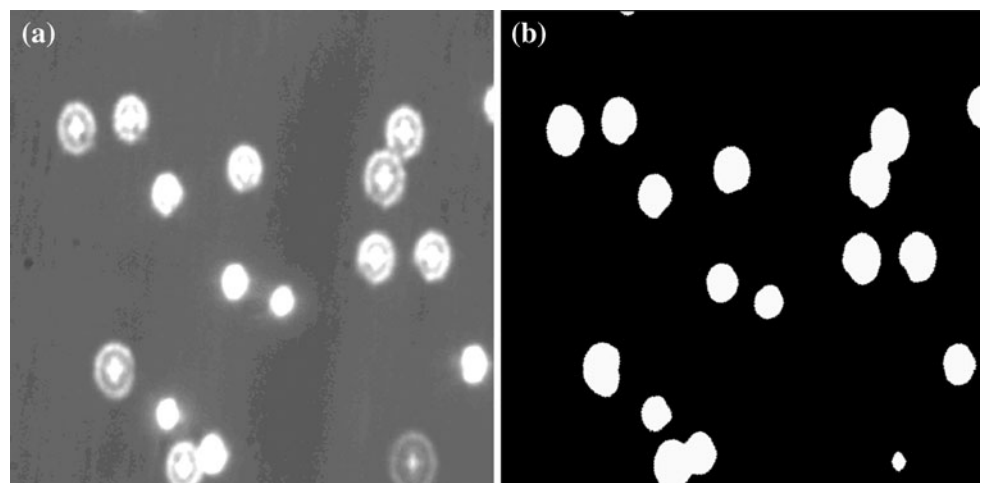
Lagrangian velocity and acceleration data. The big advantages of this technique are:

- (1) Only one optical view is needed, which simplifies the alignment and makes the technique ideally suited to examine the complex electrokinetic vortex flow with the limited single direction optical access of a microscope.
- (2) There is no loss in light intensity compared to techniques that rely on masking the optics and, what is of great importance in microfluidics, no errors due to the depth of correlation appear.
- (3) Using a high sampling rate, velocity and acceleration information are available during the whole measurement time and transient effects can be investigated.

In Fig. 3, original images of the experiment are shown. The elliptical shape of the particle images can be clearly seen (Fig. 3a). Image preprocessing is applied to the images in order to determine regions containing particle images are present. First a background reduction and later a

segmentation according to a certain gray value threshold is performed (Fig. 3b). In these initially identified regions, the x - and y -position is then determined by applying a wavelet algorithm with subpixel accuracy on the original images. This algorithm showed better results than two one-dimensional Gaussian fits that were originally used by Hain and Kähler (2006). For details about the wavelet algorithm, the interested reader is referred to Cierpka et al. (2008). For the determination of the depth position, the particle's image width and height are calculated using the autocorrelation function (Hain et al. 2009). The use of the autocorrelation was shown to make the algorithm robust and applicable to the noisy images typically found in microfluidic investigations. The random background noise for the images of the current experiment was found to be just 7% of the signal. For this low noise level, the error made by the algorithm is 1% for the axis ratio and 0.05 pixels for the position. Considering the framing time for the camera to be exact, this results in an error of $\pm 0.063 \mu\text{m/s}$ for the velocity in the (x, y) [or equivalently the (r, θ)] plane and a

Fig. 3 **a** Original images of tracer particles viewed using wavefront deformation. **b** The same image after segmentation. The defocusing effect can clearly be seen



maximum error of $\pm 2.3 \mu\text{m/s}$ for the velocity in viewing direction. For more details about the technique and the image processing, the interested reader is referred to (Cierpka et al. 2010b).

The calibration in the x - and y -direction was done by imaging a microscopic scale and relating a distance in image space to a distance in object space. The next step for the reconstructing the motion of the tracer particles was to calibrate the elliptical shape of the particles with respect to position perpendicular to the focal plane. The calibration was done by changing the z -position of a microscope slide with particles stuck to the wall in steps of $1 \mu\text{m}$. To allow for the calibration performed of dried samples in air, the z -positions for measurements of EMV were multiplied by the refractive index of water ($n_w = 1.3$). Figure 4 shows the evolution of the image width and height versus the z -position. The graphs show focal planes with a minimum at $z \approx 0 \mu\text{m}$ for a_y and $z \approx 6 \mu\text{m}$ for a_x . Usually the measurement volume depth is given by distance between the two focal planes. Nevertheless, measurements are possible due to the high signal-to-noise ratio and uniform diameter of the particles. The width to height ratio, $a_{xy} = a_x/a_y$, is unambiguous in the range of $z = 0\text{--}25 \mu\text{m}$. Chen et al. (2009) used the difference between width and height $a_x - a_y$ for the calibration. In this study, both values the ratio a_{xy} , and the difference $a_x - a_y$ are used in combination with the absolute width a_x and height a_y of the tracer particles to increase reliability. By comparing the different values, the best estimate for the depth is chosen. The estimated depth position z_{est} is also plotted in Fig. 4 and shows good agreement with the absolute position z . In the region of the actual microvortex ($z = 29\text{--}55 \mu\text{m}$, indicated in gray) the standard deviation of the calibration

was $\sigma_z \sim 1.3 \mu\text{m}$. The uncertainty for a confidence interval of 90:1 can be estimated to be $2\frac{\sigma_z}{dt} \approx 12 \mu\text{m/s}$. Since the data was recorded with equidistant time intervals (dt) and information from previous time steps were taken into account for the evaluation, the actual uncertainty of the measurements will be much lower than the estimate with the calibration data.

Using the calibration information, the three-dimensional position of a tracer particle is determined for an image at time t_1 . By a nearest neighbor approach, the corresponding particle image is found in the next image at time t_2 and the radial, angular and axial velocity components (u_r, u_θ, u_z) can be estimated. As is typical for PTV, the seeding density is low. To use the nearest neighbor approach, best results are obtained if the displacement between the two successive positions of a particle is lower than 20% of the mean distance between particle images (Malik et al. 1993). Since the measurements are time resolved, additional information from other time steps could also be used, allowing the seeding density to be significantly increased. However, for the present manuscript this was not necessary. Particles that belong to the same trajectory were reliably identified. Tracer particles are introduced into the channel, prior to initiation of the EMV. Subsequently the electric field and laser are both applied. The viewing plane is located at the top electrode and since the same objective lens serves both as the viewing and laser focusing lens, the laser is also focused at the top electrode. As soon as the laser illumination and electric field are both initiated, the particles are transported by the EMV and start moving in closed orbits. As the particles move in closed orbits they approach and recede from the focal plane. In the imaging plane, this motion can be seen in the form of the changing elliptical shape of the particle image (Supporting Movie 1). Due to the axisymmetric three-dimensional nature of the EMV, the motion in the viewing plane (and parallel planes) is primarily radial, but in the z -direction, significant motion exists. Figure 5 depicts the tracer pathlines from a top view. In Fig. 5a, the measured particle positions are shown. The measurement time, ranging from $t = 0$ to 140 s is color coded. Note the bigger gaps between the particle positions close to the center of the vortex ($x \approx 220 \mu\text{m}$; $y \approx 150 \mu\text{m}$), where the velocity is higher. Radial distances, r , in the rest of the work indicate distances from this center measured perpendicular to the optical axis (z -direction). Some of the trajectories could be resampled over the whole measurement time. In Fig. 5b, particle positions belonging to the same trajectory are plotted with the same color. For this particular measurement ($F = 200 \text{ kHz}$) 558 different trajectories were found. Since overlapping particle images are filtered out and particles can leave the field of view, some trajectories have gaps and are interpreted as new trajectories at a later time instant.

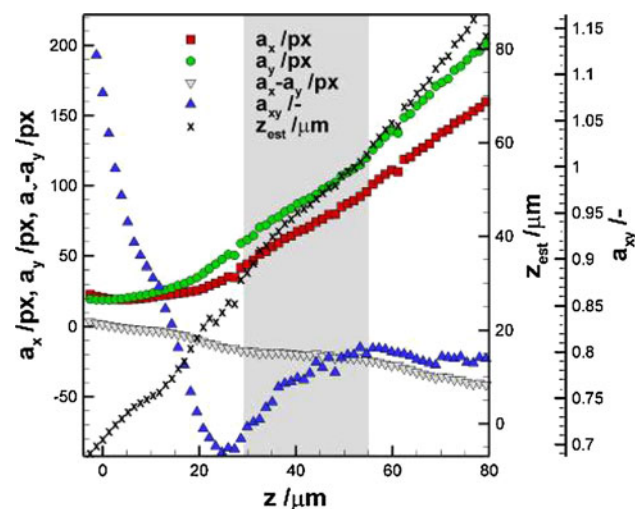


Fig. 4 The absolute width and height a_x, a_y , the difference $a_x - a_y$, the ratio a_{xy} and the estimated depth z_{est} versus the real depth position z . Highlighted in gray is the region of the vortex roll

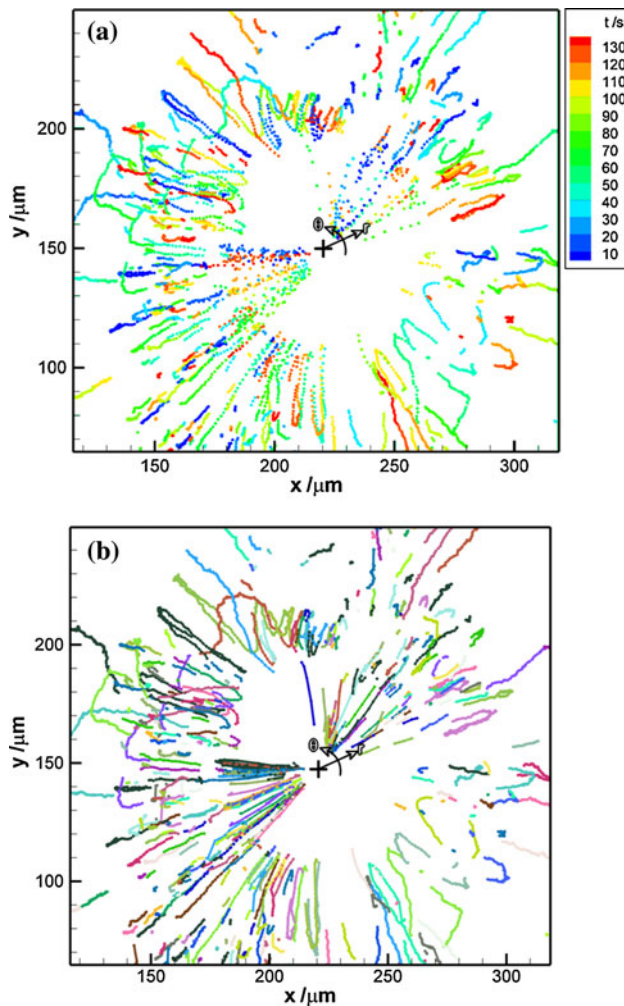


Fig. 5 **a** Top view of the particle pathlines ($F = 200$ kHz). Color coded is the time of measurement. **b** Trajectories, indicated by different colors found by the PTV algorithm. (Color figure online)

Assuming local smoothness of the particle trajectories, a spline fit was applied to the data. Reliable information about the velocity and the acceleration at every time instant can be found by this procedure. Using this procedure measurements for three different driving AC frequencies ($F = 100, 200, 300$ kHz) over 140 s could be performed successfully.

2.3 Numerical simulations

Electrothermal fluid flow occurs due to the action of the electric field on the gradients in the medium, which in turn are induced by temperature gradients. This action of the electric field on the gradients in the medium can be taken into account by introducing in the fluid transport equations, an electrothermal body force term given by (Green et al. 2001)

$$\langle f_e \rangle = \frac{1}{2} \text{Re} \left[\frac{\sigma \varepsilon (\alpha - \beta)}{\sigma + i \omega \varepsilon} (\nabla T \cdot \mathbf{E}) \mathbf{E}^* - \frac{1}{2} \varepsilon \alpha |\mathbf{E}|^2 \nabla T \right] \quad (1)$$

where $\text{Re}(\dots)$ denotes the real part of the expression, T is the temperature, \mathbf{E} is the electric field vector, \mathbf{E}^* is the complex conjugate of the electric field vector, ω is the angular frequency of the applied electric field, k and σ are the thermal and electrical conductivities, and α and β are the fractional changes of ε and σ with temperature given by $1/\varepsilon(d\varepsilon/dT)$ and $1/\sigma(d\sigma/dT)$, respectively. For an aqueous electrolyte solution, typically $\alpha \approx -0.4\% \text{ K}^{-1}$ and $\beta \approx 2\% \text{ K}^{-1}$. The first term in Eq. 1 is the Coulomb force and the second term is the dielectric term and both the terms depend on the local temperature gradient (∇T). Gradients in the permittivity and conductivity of the fluid also determine the magnitude of the body force. Equation 1 also shows that the body force term is dependent on the AC frequency, but in the range of AC frequencies chosen in this work, the body force does not change appreciably (Kumar et al. 2010b). In general, for hydrodynamic simulations involving such electrothermal forces the electric, temperature and velocity fields are coupled. It can be shown that in microsystems such as ours, heat transport due to thermal diffusion dominates over convection, implying that the temperature and velocity problems are decoupled (Morgan and Green 2003). If the local temperature gradients are known then the electrothermal body force can be estimated, and subsequently solving the Navier–Stokes equation would yield the velocity field.

Estimating the local temperature gradients produced by the focused laser illumination (Fig. 1) is, however, not straightforward. This is so because the laser illumination can potentially heat the substrates and the liquid, and an accurate knowledge of the fraction of heat absorbed by the different components of the microfluidic device would be required to estimate the temperature field. In a recent investigation, Kumar et al. (2010b) showed that for the combination of an IR laser (1064 nm) and ITO electrodes, heating of the electrode substrate is the primary means of temperature gradient creation. Using laser-induced fluorescence thermometry (LIF) Kumar et al. (2010b), were able to measure the temperature field at the fluid, electrode interface. Their experimentation suggests the use of the simplified model to account for the heating—accounting for the laser heating by simply imposing temperature boundary conditions (Fig. 6). The heating of the fluidic medium itself is neglected. Under these assumptions, the temperature profiles at the boundary were estimated and extrapolated from previous experimentation (Williams 2009; Kumar et al. 2010b). The EMV motion was simulated with Comsol Multiphysics® (Stockholm, Sweden). The simulated volume is two-dimensional axi-symmetric, where the optical axis serves as the axis of symmetry

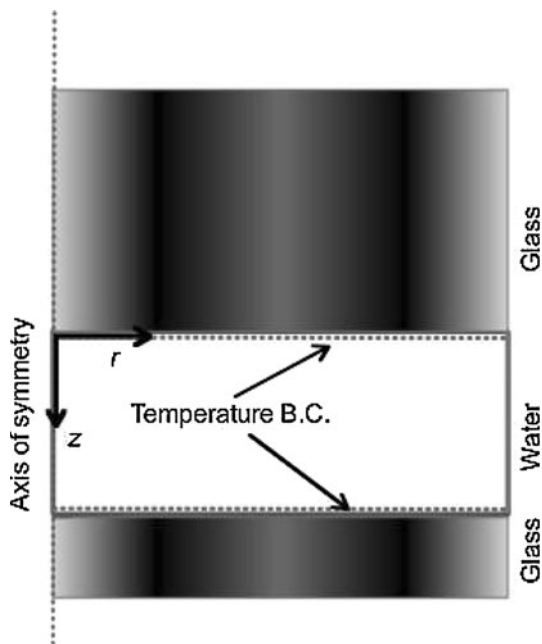


Fig. 6 A schematic of the problem space for numerical simulations. The optical axis defines the axis of symmetry. Heating by the laser is accounted for through the temperature boundary conditions

Table 1 Values of different computational parameters

Computation parameter	Value
Computational domain ($z \times r$)	$50 \mu\text{m} \times 5000 \mu\text{m}$
$T(z = 0)$	$300.9 + \frac{60445}{(2r)^2 + 94.9^2}$, r measured in μm
$T(z = 50 \mu\text{m})$	$300.5 + \frac{30223}{(2r)^2 + 94.9^2}$, r measured in μm
Applied AC voltage	8.9 V _{pp}
Applied AC frequency	200 kHz
Medium conductivity (σ)	38 mS/m
Medium permittivity (ϵ)	$80 \times (8.854 \times 10^{-12})$ F/m

(Fig. 6). The computational domain is meshed to achieve grid independence. The simulation is carried out in three steps: first the electric field is calculated, then the resulting thermal field is calculated, and finally the induced fluid flow velocity was found from the Navier–Stokes equation (u_r, u_z). The values of some of the computational parameters used are tabulated in Table 1.

3 Results

Figure 5 depicts the recovered tracer locations, in the plane of visualization, during the entire measurement period for $F = 200$ kHz. As can be seen in Fig. 5a, the velocity of the tracer particles increases significantly as the vortex center

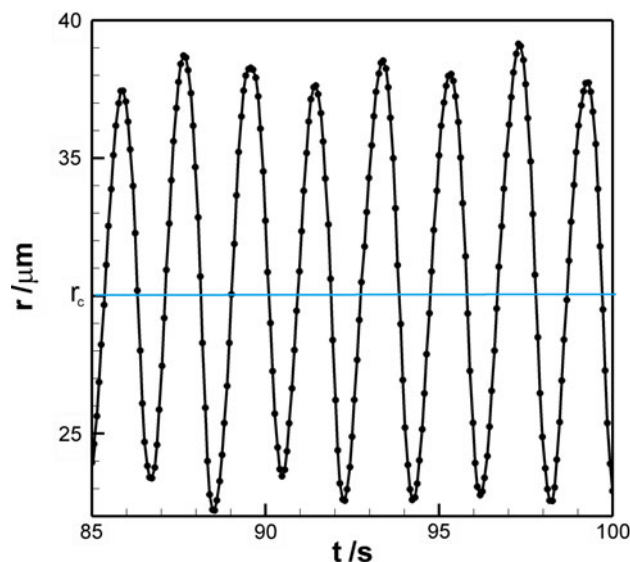


Fig. 7 Radial location of a selected particle as a function of time ($F = 200$ kHz). The time axis represents the global time (time since measurement was initiated). It can be seen that the particle is oscillating about a non-zero radial location from the laser focus, which has been denoted as r_c . In the (r, z) plane, r_c can be regarded as the distance from the origin to the center of the vortex roll

is approached. Hence, distance between the successive particle positions becomes much larger towards the center. The PTV algorithm is able to recover individual trajectories as shown in Fig. 5b. The individual trajectories reveal that the motion in the viewing plane is primarily radial with a small angular component ($\frac{u_\theta}{u_r} < 0.1$). As the particles approach the vortex center, a large axial velocity component develops, which accounts for the lack of trajectories close to the vortex center. The temporal evolution of a selected particle trajectory is depicted by Fig. 7. As can be seen, the tracer particle can be regarded to be in periodic motion about a particular radial location. This radial distance, which also is the distance of the center of closed trajectories from the optical axis, will be denoted by r_c and later on will serve as length scale associated with the EMV.

The wavefront deformation PTV is capable of resolving the motion in the axial direction, without the need to traverse the plane of visualization. By recovering the shape encoded axial position of the tracer particles, the full 3-D nature of the EMV could be determined (Fig. 8). For clarity, Fig. 8 depicts only a partial set of pathlines. These pathlines are color coded to also represent the radial velocity component. The toroidal nature of the vortex flow can be clearly seen. It can also be seen that the size of the orbits might change for a certain particle during several revolutions. Furthermore, the radial movement away from the vortex center is faster ($|u_r| \sim 30 \mu\text{m/s}$) than the radial movement towards the center ($|u_r| \sim 20 \mu\text{m/s}$). A small angular component of the velocity causes the particles to

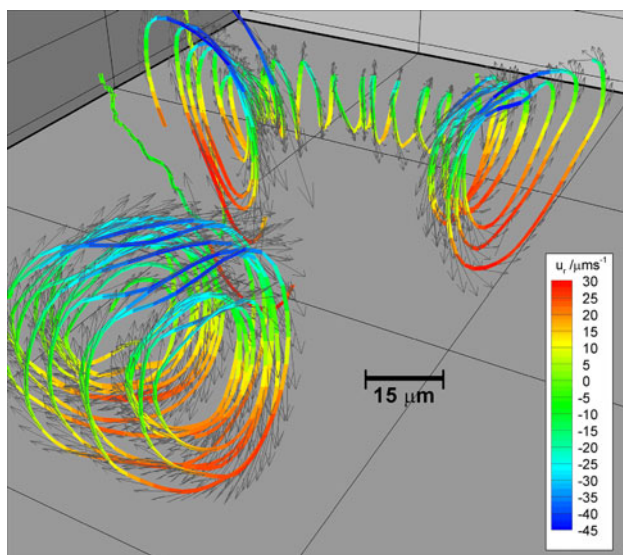


Fig. 8 Three-dimensional particle trajectories and corresponding velocity vectors in the vortex center ($F = 200$ kHz). Color represents the radial velocity component. The optical axis (not shown) lies centrally. (Color figure online)

drift slightly around the vortex center, even while rotating in the (r, z) plane. This drifting motion is possibly caused by pressure fluctuations or other low-frequency vibrations not associated with the electrothermal body forces.

These measurements also enable the computation of the Lagrangian velocity vectors associated with the tracer displacement. The raw velocity vectors that are obtained correspond to the (r, θ, z) space. However, since the system is axially symmetric with negligible angular velocities, all velocity vectors can be projected into the (r, z) plane without loss of information. Figure 9 depicts the vortex velocity vectors and trajectories for $F = 200$ kHz, where the motion is projected onto the (r, z) plane. In Fig. 9a, the velocity vectors are shown, color coded according to the axial velocity component. The trajectories span approximately $25 \mu\text{m}$ and the center of the closed trajectories lies approximately at a radial distance of r_c ($\sim 30 \mu\text{m}$) from the vortex center or optical axis. The shape of the trajectories is not circular, but they are skewed. This effect is caused by the differential heating at the lower and upper electrodes, due to focusing of the IR laser at the top electrode. Our illumination setup causes stray IR illumination, an artifact of the holograms used to generate the illumination lying $\sim 70 \mu\text{m}$ radially from the primary focused IR beam. This along with continuity reasons creates a secondary slower vortex, as can be seen for locations with $r > 50 \mu\text{m}$ in Fig. 9. Particles were never exchanged between the primary and secondary vortices, and the two vortices are also separated by a slightly tilted sharp border. Figure 9a also shows that close to the optical axis ($r \sim 0 \mu\text{m}$) particles move in the positive z -direction with high axial velocities

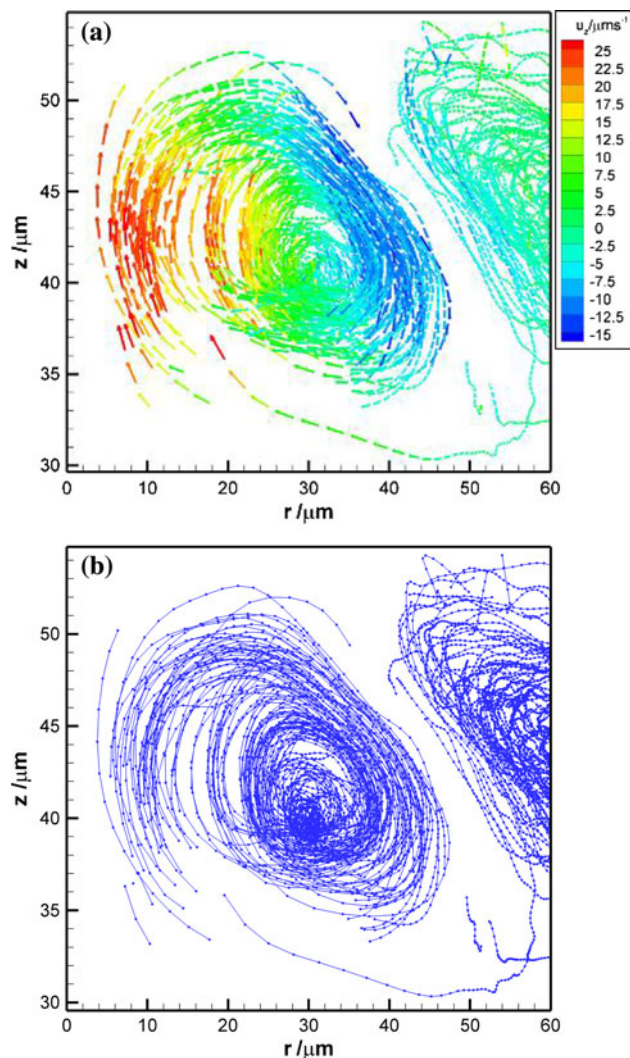


Fig. 9 a Velocity vectors in the rz -representation ($F = 200$ kHz). Color coded is the axial velocity component. **b** Trajectories for different driving frequencies. Note, that the z -axis is stretched for better readability. (Color figure online)

($|u_z| \sim 25 \mu\text{m/s}$). The downward motion close to the vortex edge ($r \sim 50 \mu\text{m}$) is slower ($|u_z| \sim 15 \mu\text{m/s}$) due to continuity reasons. Figure 9b shows trajectories from measurements at 200 kHz AC frequency. The vortex shape does not change qualitatively with AC frequency, i.e. 100, 200, and 300 kHz (data not shown), which agrees with the previous two-dimensional fluid flow visualization (Kumar et al. 2009). Even the length scale associated with the vortex (r_c) remains the same. However, for $F = 300$ kHz, the average velocity in the vortex decreases, which agrees with the theory (Morgan and Green 2003).

Figure 10 depicts the variation of the axial and radial velocity components with radial distance from the optical axis for the case of 200 kHz AC frequency. The axial velocity (u_z) initially decreases linearly with r (Fig. 10a). It vanishes at the core of the torus ($r = r_c$) and decreases

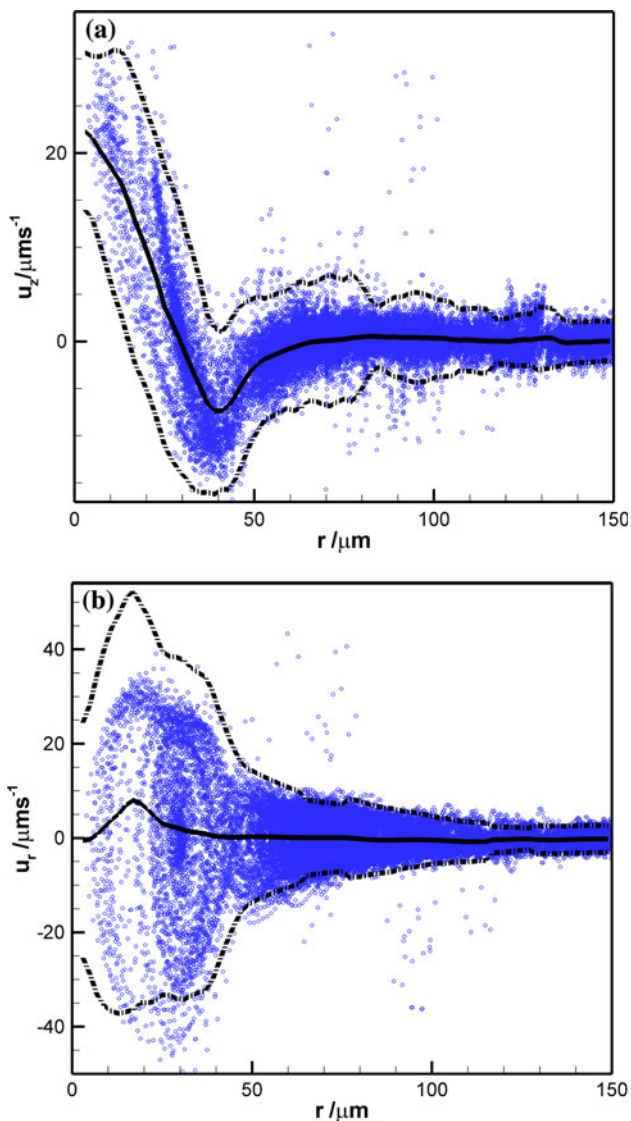


Fig. 10 Experimentally measured velocities for $F = 200$ kHz. The *blue dots* indicate experimental measurements, while the *solid black line* indicates the average and the *dashed black lines* indicate twice the standard deviation. **a** Axial velocity component versus radius. **b** Radial velocity component versus radius. (Color figure online)

further to a minimum of $u_z = -15 \mu\text{m/s}$ at $r = 40 \mu\text{m}$. With further increase in radial distance, u_z increases until it again vanishes. In Fig. 10b, we can see that the velocity data is approximately symmetrically distributed about $u_r = 0 \mu\text{m/s}$. With the increasing radial distance, u_r decreases in absolute magnitude and eventually vanishes at large radial distances. These velocity profiles can be used to calculate the effect of fluid transport in the different microfluidic applications involving the EMV (e.g., REP).

These experimentally obtained velocity distributions were compared with numerical simulations. Before comparison, the spatial coordinates r and z were normalized with the length scale associated with the EMV, i.e., r_c . r_c

obtained from experimental data was $\sim 30 \mu\text{m}$, whereas with numerical simulations it was found to be $60 \mu\text{m}$. Moreover, the z height is translated so that the center of the vortex roll now is at $z' = 0$. In Fig. 11a, the streamlines from the numerical data are shown together with numerically obtained contours of the axial velocity. Figure 11b depicts experimentally observed pathlines overlaid on numerically obtained contours of the axial velocity. The comparison is reasonably good, even though the streamlines from numerical computations indicate quite a large torus. However, pathlines obtained from PTV analysis are closed at $r/r_c = 1.5$. This is so because the stray IR illumination is not accounted for in numerical computations. Moreover, the inertia of our tracer particles can be expected to cause variation between experimental data and numerical simulations. Nevertheless, the tilt observed with experimental pathlines (Fig. 11b) is also seen in numerical simulations (Fig. 11a). A comparison between experimentally obtained velocities and velocities obtained from

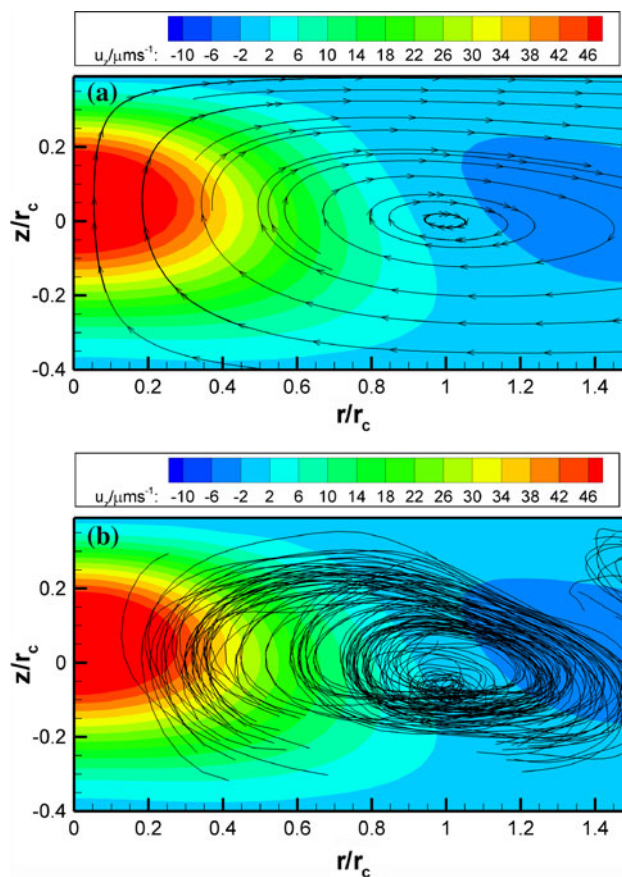


Fig. 11 Comparison of numerical simulations and experimental results. Note that data have been normalized by their respective vortex length scales. **a** Streamlines obtained from numerical simulations plotted in normalized coordinates. *Contours*, obtained from numerical data, represent the axial velocity component. **b** *Pathlines* obtained from experimental data are superposed over contours obtained from numerical data

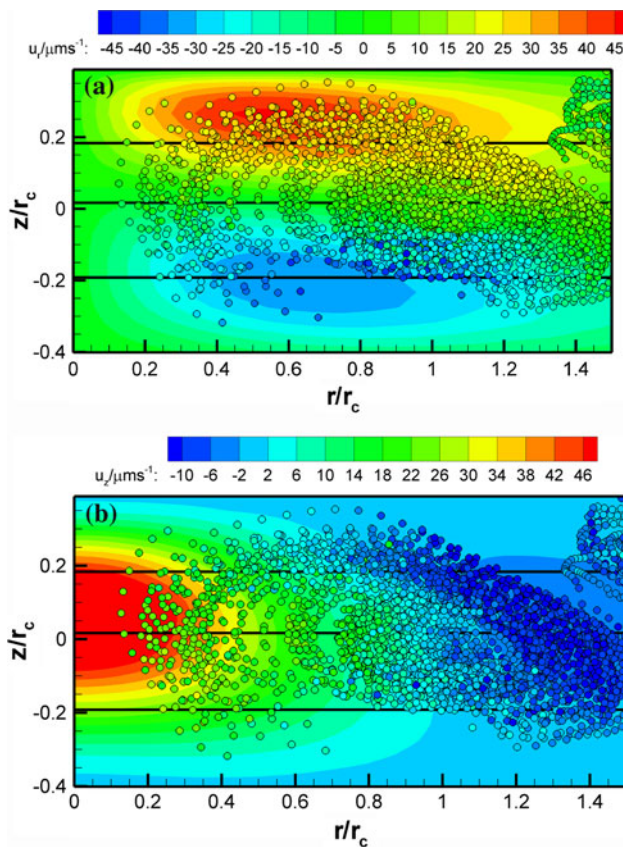


Fig. 12 **a** The scatter plot obtained from experimental data is superposed over a contour plot, obtained from numerical simulations. Both the *scatter* and *contour* plots represent the radial velocity component. **b** Similar to **a**, expect that the axial velocity components are now represented

numerical computations is provided in Fig. 12. In Fig. 12a and b, the contours represent radial and axial velocities obtained from the numerical computation, respectively, while the color of the circles represents the corresponding value of experimental data. Figure 12a shows that the comparison for radial velocity is good. For the case of axial velocity, slight differences exist between experimental measurements and numerical predictions (Fig. 12b). Especially in the regions of high velocities and high velocity gradients, absolute value of the particle's axial velocity is always lower than predicted by the numerical simulation. Such differences can be expected on account of the inertia of the large tracking particles used.

Figure 13 provides more quantitative comparison between experimental findings and numerical simulations. Figure 13a depicts the three cross-sections at which comparisons are made. Overall, both radial and axial velocities appear to compare well (Fig. 13b, c). The experimentally obtained radial velocity yields distributions that compare very well with simulations (Fig. 13b). Numerical simulations predict high axial velocities close to the vortex center,

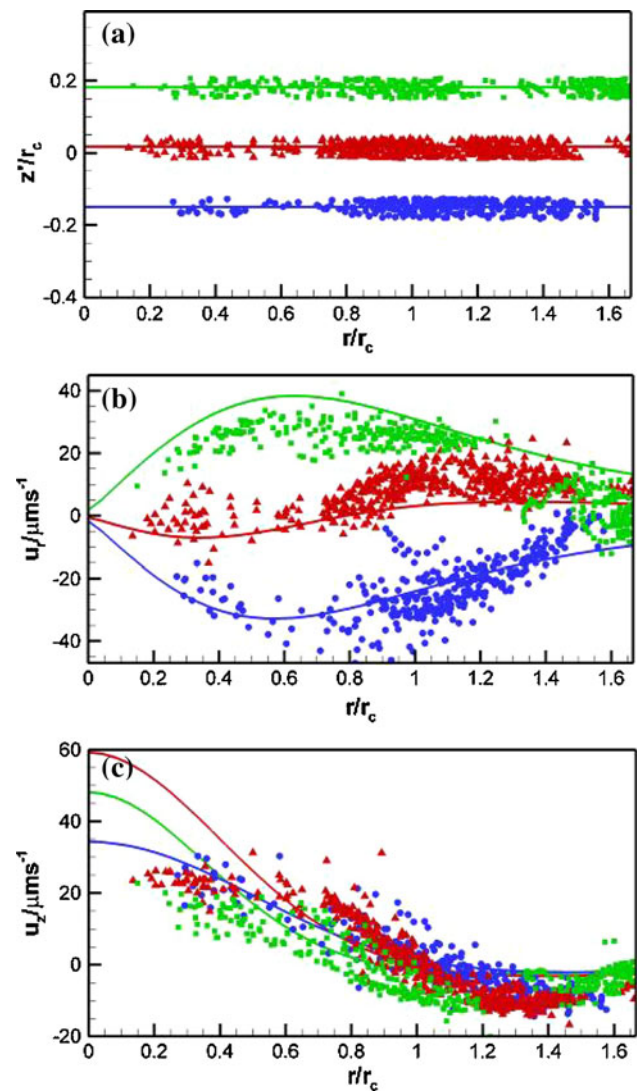


Fig. 13 **a** Lines indicate sections at which velocities from simulation data are obtained. Scatter plots indicate corresponding locations at which velocities from experimental data are obtained. **b** Radial velocity profiles. **c** Axial velocity profiles

where experimental data is sparse and is typically lower in magnitude as compared to simulations (Fig. 13c). To investigate this issue, further studies should focus on altering the current configuration to allow for smaller tracer particles and higher seeding densities.

4 Conclusions

We showed that the 3D3C wavefront deformation particle tracking, which was developed at Universität der Bundeswehr, is easily adaptable to conventional microscopy hardware. The measurement range could be extended beyond the two in-focus planes by taking the ratio and the difference of width and height into account. Using this

technique we were able to investigate an EMV in a shallow channel with high z -velocity gradients without traversing the viewing plane. We also showed that the experimentally observed flow structure is corroborated by numerical simulations. Once numerical data is validated it gives access to a broader range of variables and can help to better understand the flow phenomena.

5 Outlook

For the numerical simulations, the boundary conditions are of crucial impact. Therefore, further investigations about the temperature profile in the micro channel have to be performed. The three-dimensional structure of the microvortex under study plays an extremely important role in many microfluidic applications. A complete investigation of the three-dimensional fluid flow will further the understanding of the role of electrothermal fluid transport in these applications.

Acknowledgments A. Kumar acknowledges support from the Bilsland Dissertation and the Josephine De Kármán Fellowships. Financial support from Deutsche Forschungsgemeinschaft (DFG) in frame of the priority program SPP 1147 is gratefully acknowledged by C. Cierpka.

References

- Chen S, Angarita-Jaimés N et al (2009) Wavefront sensing for three-component three-dimensional flow velocimetry in microfluidics. *Exp Fluids* 47(4–5):849–863
- Choi Y, Lee S (2010) Holographic analysis of three-dimensional inertial migration of spherical particles in micro-scale pipe flow. *Microfluid Nanofluid*. doi:10.1007/s10404-101-0601-8
- Cierpka C, Weier T, Gerbeth G (2008) Evolution of vortex structures in an electromagnetically excited separated flow. *Exp Fluids* 45(5):943–953
- Cierpka C, Hain R, Kähler CJ (2009) Theoretical and experimental investigation of micro wavefront-deformation particle tracking velocimetry. In: 8th international symposium on particle image velocimetry—PIV09 2009, Melbourne, Australia
- Cierpka C, Rossi M, Segura R, Kähler CJ (2010a) Comparative study of the uncertainty of stereoscopic micro-PIV, wavefront-deformation micro-PTV, and standard micro-PIV. In: International symposium on applications of laser techniques to fluid mechanics (LISBON2010), Lisbon, Portugal
- Cierpka C, Segura R, Hain R, Kähler CJ (2010b) A simple single camera 3C3D velocity measurement technique without errors due to depth of correlation and spatial averaging for microfluidics. *Meas Sci Technol* 21(4):045401.1–045401.13
- Green NG, Ramos A, Gonzalez A, Castellanos A, Morgan H (2000) Electric field induced fluid flow on microelectrodes: the effect of illumination. *J Phys D* 33(2):L13–L17
- Green NG, Ramos A, Gonzalez A, Castellanos A, Morgan H (2001) Electrothermally induced fluid flow on microelectrodes. *J Electroanal Chem* 53(2):71–87
- Hain R, Kähler CJ (2006) Single camera volumetric velocity measurements using optical aberrations. In: 12th international symposium on flow visualization, Gottingen, Germany
- Hain R, Kähler CJ, Radespiel R (2009) Principles of a volumetric velocity measurement technique based on optical aberrations. Notes on numerical fluid mechanics and multidisciplinary design. Springer-Verlag, Berlin
- Kumar A, Williams SJ, Wereley ST (2009) Experiments on optoelectrically generated microfluidic vortices. *Microfluid Nanofluid* 6(5):637–646
- Kumar A, Chuang H, Wereley ST (2010a) Dynamic manipulation by light and electric fields: micrometer particles to microliter droplets. *Langmuir* 26(11):7656–7660
- Kumar A, Kwon J-S et al (2010b) Optically modulated electrokinetic manipulation and concentration of colloidal particles near an electrode surface. *Langmuir* 26(7):5262–5272
- Lee SJ, Kim S (2009) Advanced particle-based velocimetry techniques for microscale flows. *Microfluid Nanofluid* 6(5):577–588
- Lindken R, Westerweel J, Wieneke B (2006) 3D micro-scale velocimetry methods: a comparison between 3D- μ PTV, stereoscopic μ PIV and tomographic μ PIV. In: 13th International symposium on applications of laser techniques to fluid mechanics, Lisbon, Portugal
- Lindken R, Rossi M, Grosse S, Westerweel J (2009) Micro-particle image velocimetry (μ PIV): recent developments, applications, and guidelines. *Lab Chip* 9(17):2551–2567
- Malik NA, Dracos T, Papantoniou DA (1993) Particle tracking velocimetry in 3-dimensional flows. Part 2. Particle tracking. *Exp Fluids* 15(4–5):279–294
- Mizuno A, Nishioka M, Ohno Y, Dascalescu LD (1995) Liquid microvortex generated around a laser focal point in an intense high-frequency electric-field. *IEEE Trans Ind Appl* 31(3):464–468
- Morgan H, Green NG (2003) AC electrokinetics: colloids and nanoparticles. Research Studies Press, Philadelphia
- Peterson SD, Chuang HS, Wereley ST (2008) Three-dimensional particle tracking using micro-particle image velocimetry hardware. *Meas Sci Technol* 19(11):115406.1–115406.8
- Ragan T, Huang HD, So P, Gratton E (2006) 3D particle tracking on a two-photon microscope. *J Fluoresc* 16(3):325–336
- Satake S, Kunugi T, Sato K, Ito T, Taniguchi J (2005) Three-dimensional flow tracking in a micro channel with high time resolution using micro digital-holographic particle-tracking velocimetry. *Opt Rev* 12(6):442–444
- Sheng J, Malkiel E, Katz J (2006) Digital holographic microscope for measuring three-dimensional particle distributions and motions. *Appl Opt* 45(16):3893–3901
- Stolz W, Kohler J (1994) Inplane determination of 3D-velocity vectors using particle tracking anemometry (PTA). *Exp Fluids* 17(1–2):105–109
- Willert CE, Gharib M (1992) 3-dimensional particle imaging with a single camera. *Exp Fluids* 12(6):353–358
- Williams SJ (2009) Optically induced, AC electrokinetic manipulation of colloids. Mechanical Engineering. West Lafayette, Purdue University. Doctoral
- Williams SJ, Kumar A, Wereley ST (2008a) Electrokinetic patterning of colloidal particles with optical landscapes. *Lab Chip* 8(11):1879–1882
- Williams SJ, Kumar A, Wereley ST (2008b) Optically induced electrokinetic patterning and manipulation of particles. <http://hdl.handle.net/1813/11399>
- Williams SJ, Kumar A, Green NG, Wereley ST (2010) Optically induced electrokinetic concentration and sorting of colloids. *Micromech Microeng* 20:015022
- Yang CT, Chuang HS (2005) Measurement of a microchamber flow by using a hybrid multiplexing holographic velocimetry. *Exp Fluids* 39(2):385–396
- Yoon SY, Kim K (2006) 3D particle position and 3D velocity field measurement in a microvolume via the defocusing concept. *Meas Sci Technol* 17(11):2897–2905